

Universal Scaling Law of Glass Rheology

Shuangxi Song¹, Fan Zhu^{1,3} and Mingwei Chen^{2,3*}

¹State Key Laboratory of Metal Matrix Composites, School of Materials Science and Engineering, Shanghai Jiao Tong University, Shanghai 200030, PR China

²Department of Materials Science and Engineering, Johns Hopkins University, Baltimore, MD 21218, USA

³WPI Advanced Institute for Materials Research, Tohoku University, Sendai 980-8577, Japan

*Correspondence to: mwchen@jhu.edu.

The similarity in atomic structure between liquids and glasses has stimulated a long-standing hypothesis that the nature of glasses may be more fluid-like, rather than an apparent solid¹⁻⁴. In principle, the nature of glasses can be characterized by measuring the dynamic response of rheology to shear strain rate in the glass state. However, limited by the brittleness of glasses and current experimental techniques, the dynamic behaviours of glasses were mainly assessed in the supercooled liquid state or in the glass state within a narrow rate range. Therefore, the nature of glasses has not been well elucidated experimentally. Here we report the dynamic response of shear stress to shear strain rate of metallic glasses over nine orders of magnitude in time scale, equivalent to hundreds of years, by broadband stress relaxation experiments. The full spectrum dynamic

response of metallic glasses, together with other “glasses” including silicate and polymer glasses, granular materials, soils, emulsifiers and even fire ant aggregations, follows a universal scaling law within the framework of fluid dynamics. Moreover, the universal scaling law provides comprehensive validation of the conjecture on the jamming phase diagram by which the dynamic behaviours of a wide variety of “glass” system can be unified under one rubric parameterized by thermodynamic variables of temperature, volume and stress in trajectory space.

It has been well established that plastic flow of crystalline materials is predominantly driven by the formation/motion of discrete crystal defects such as vacancies, dislocations, stacking faults, twins and grain boundaries in various stress, time and temperature domains ⁵. This is fundamentally different from that in simple or complex liquids which behave in viscous or viscoelastic fashion. While, unlike crystals, stiff and hard glasses, such as metallic glasses (MGs) and window (oxide) glasses, usually have liquid-like disordered atomic/molecular structures and do not have geometrically well-defined defects with a static atomic/molecular configuration for plastic deformation. It has been long conjectured that glasses may retain the nature of liquids as suggested by some peculiar glass flowing observations from thickened bottoms of stained glass panes in old European churches ⁶. Physically, the nature of glasses can be characterized by correlating the dynamic response of plastic flow to applied force. Under quasi-static loading conditions at room temperature, plastic rheology of glasses is usually considered being associated with the collection of local

shearing events. For MGs, the local shearing is described by a dynamic variable, shear transformation zone (STZ), which represents the evolution of shear-induced local configurations in the disordered system⁷⁻¹². The experimentally accessible parameter, which can microscopically depict the plastic flow of MGs, is the statistical size of STZs. Depending on theoretical models and experimental methods, the estimated STZ volumes have been reported to vary over two orders of magnitude from several atoms to hundreds of atoms¹³⁻¹⁶, which is far beyond possible experimental errors. In fact, the large discrepancy in STZ volumes has caused intense debate and confusion on the understanding of rheology mechanisms in MGs. We noticed that previous experiments were carried out within a limited strain rate range and different time domains. The dispute of rheology behaviour may arise from a distinct rate/time dependence of flow mechanisms, although mechanical behaviour of MGs is usually considered time insensitive at temperatures far below glass transition points (T_g) according to the conventional wisdom. Thus, to develop a thorough understanding of the rheology of MGs and thus the nature of the hard glasses, it is necessary to design and carry out experiments that are capable of measuring the dynamic response of MGs over a broad strain-rate range.

As shown in **Figure 1a** we measured the dynamic shear stress response of a $Zr_{55}Cu_{30}Al_{10}Ni_5$ MG¹⁷ at shear strain rates ranging from 10^{-8} to 10^0 s⁻¹ using both broadband nanoindentation and cantilever bending methods. In the stress relaxation experiments, shear strain rate ($\dot{\gamma}$) and nominal shear stress (τ) are derived from the contact force (P) and displacement (h) at different relaxation time (t) (see

Methods). The estimated shear stress is plotted as the function of shear strain rate for the high-rate nanoindentation (**Fig. 1b**) and low-rate cantilever experiments (**Fig. 1c**). The experimental data points obtained by two different methods perfectly overlap with each other in the strain rate range between $\sim 10^{-6}$ and 10^{-5} s^{-1} and form one completely smooth curve (**Fig. 2a**). For the first time, the dynamic mechanical response of MGs is presented in such a wide rate range from $\sim 10^{-8}$ to 10^0 s^{-1} , spanning nine orders of magnitude in time scale. Converting into a log-log plot, there are two distinct linear regions with two dramatically different slopes, *i.e.* strain rate sensitivities ($m = \partial \ln \tau / \partial \ln \dot{\gamma}$), at high and low strain rates (stresses), respectively. In the transition region, there is a rapid change of strain rate sensitivity from 0.004 to 1.0 occurring within a narrow strain rate range between 10^{-4} and 10^{-6} s^{-1} (inset in **Fig. 2a**). At high strain rates ($> 10^{-4} \text{ s}^{-1}$), the experimental data can be well fitted by Johnson-Samwer cooperative shear mode (CSM) portrayed by a sinusoidal function of megabasin potential energy density ⁹:

$$\dot{\gamma} = \dot{\gamma}_0 \exp\left(-\frac{W_{CSM}}{kT}\right) \quad (1)$$

where $\dot{\gamma}_0 \approx 10^{10} \text{ s}^{-1}$ is the elastic strain rate limit ⁹, W_{CSM} is the activation energy of cooperative shear, which depends on stress (*see Methods*); k is the Boltzmann constant and T is temperature. On the other hand, at the strain rates below 10^{-6} s^{-1} , the flow rate follows a power law with a rate sensitivity or power index of unity. In this case, the rate-stress dependence can be described by Spaepen-Argon equation, originally derived from the transition state theory (TST) ^{7,8}:

$$\dot{\gamma} = \alpha \gamma_0 \nu_G \exp\left(-\frac{W_{STZ}}{kT}\right) \sinh\left(\frac{\tau \gamma_0 \Omega}{2kT}\right) \quad (2)$$

where α (of order unity) is the steady-state volume fraction of flow units contributing to plastic flow; γ_0 represents the transformation strain of STZs and is taken as 0.125; $\nu_G \approx 10^{13} \text{ s}^{-1}$ is the intrinsic phonon relaxation time¹⁸; W_{STZ} and Ω are the activation energy and volume of STZs⁷. The activation energy and size of STZs by fitting the strain rate data in **Fig. 1d** and **2a** using **Equations (1)** and **(2)** are listed in **Extended Data Table 1**. The STZ size at high stresses is determined to be $\sim 5.64 \text{ nm}^3$ or 338 atoms by CSM, consistent with previously reported rate-jump measurements of Zr-based metallic glasses at high stresses and strain rates¹⁴. The activation energy for the cooperative shear is estimated to be 5.91 eV, close to that for the α relaxation¹⁹. In contrast, the STZ volume at low stresses is measured to be only $\sim 0.22 \text{ nm}^3$ or 16 atoms at low stresses, consistent with previous relaxation spectrum measurements¹³ as well as those measurements at temperatures close to T_g ¹⁶. Correspondingly, a low activation energy of only $\sim 1.08 \text{ eV}$ and small activation volume (V^*) of 0.028 nm^3 or a single atom by $V^* = \gamma_0 \Omega$ are obtained from the TST equation. Both the activation volume and activation energy indicate that dynamic flow of the MG at low strain rates can be described by single atom motion or synchronized motion of all atoms at the same pace. In particular, the linear correlation between shear stress and shear strain rate at rates below 10^{-7} s^{-1} indicates that the MG follows the behaviour of a Newtonian liquid at low rates.

In the transition region, the strain rate sensitivity drops sharply from ~ 1.0 to 0.004 within a narrow strain rate range between 10^{-6} and 10^{-4} s^{-1} , accompanied by significant increases in flow stresses, activation energy and STZ volume, showing a strong rate-dependent non-Newtonian behaviour. The dynamic response of the MG in this region cannot be explained by either irreversible Johnson-Samwer cooperative shear or reversible Spaepen-Argon stochastic theory. Instead, the data in this region can be best fitted by Kohlrausch (or stretched exponential) relaxation function as shown by the black line in **Fig. 2a** and **Extended Data Fig. 1** (*see Supplementary Information*). The good agreement with the Kohlrausch relaxation function suggests that the dynamic response in the transition region involves many-body interactions^{20,21}. It is in great contrast to CSM for fast relaxation and TST for slow relaxation, both can be essentially described by a single body process.

On the basis of the shear stress and shear strain rate measurements in **Fig. 2a**, the viscosity ($\eta = \tau/\dot{\gamma}$) of the MG is calculated and plotted as the function of strain rate in **Extended Data Fig. 2**. The Newtonian viscosity (η_N) of the MG is estimated to be $\sim 8.5 \times 10^{14} \text{ Pa}\cdot\text{s}$ at room temperature. The viscosity of the MG at room temperature and literature data of other Zr-based MGs achieved at high temperatures near T_g ²² are plotted in **Extended Data Fig. 3a**. The viscosity data are normalized by Newtonian viscosity at each temperature and plotted as a function of strain rate in **Extended Data Fig. 3b**. The relationship between normalized viscosity (η/η_N) and strain rate of all data show the same trend from Newtonian flow at low strain rates to shear thinning at high strain rates. The normalized viscosity from current study and literature data are

further plotted as the function of the scaled shear strain rate ($\dot{\gamma}\eta_N$), *i.e.* viscous stress in Newtonian flow (**Fig. 2b**)²²⁻²⁶. It is immediately evident that all the data fall on one master curve that spans a wide shear strain rate regime from 10^{-9} to 10^6 s⁻¹, independent of temperatures (below or above T_g , *i.e.* glass or liquid states), chemical composition and sample geometry.

We noticed that the similar dynamic trend of normalized viscosity as the function of scaled strain rate can also be obtained from a wide range of “glass” systems, including inorganic glasses²⁷, polymer glasses²⁸⁻³⁰, emulsifiers³¹, granular materials³², soil liquefaction³³, and even fire ant aggregations³⁴ (**Fig. 2c**). However, their viscous stresses (*i.e.* $\dot{\gamma}\eta_N$) vary several orders of magnitude in these “glass” systems. Based on the universal scaling law for the yield strength of glasses, $\tau_C = 3k(T_g - T)/V$,

developed in our previous study³⁵, the normalized viscosity is further plotted as the function of a dimensionless parameter $\dot{\gamma}\eta_N \frac{V}{3kT_g}$ in **Fig. 2d**, where V is the average

molar volume determined from average atomic or particulate weight M and density ρ ,

i.e. $V = M/\rho$ (see **Extended Data Table 2**). $\dot{\gamma}\eta_N \frac{V}{3kT_g}$ is equivalent to $\frac{\dot{\gamma}\eta_N}{\tau_C} = B_i$,

where B_i is the Bingham number defined as the ratio of the viscous stress ($\dot{\gamma}\eta_N$) to the elastic shear stress limit (*i.e.* yield strength) τ_C of liquids at $T = 0$ K with a molar

volume V ³⁶. It is remarkable that the experimental data from all “glass” systems fall within a close proximity of one master curve in **Fig. 2d**, demonstrating that *the dynamic response of the “glass” systems obeys a universal scaling law within the framework of*

the classical fluid dynamics. This is the first time that *the rheology of a wide variety of disordered systems is unified by a single scaling law*.

The scaled rheological behaviour exhibits two linear regimes with distinct slopes in the double-log plot (**Fig. 2d**). The slope is zero at low rate Newtonian flow region, suggesting a rate-independent property of equilibrium liquids. By contrast, at the high flow rate or high viscous stress region, the slope gradually approaches to -1, indicating an elastic-plastic rheological behaviour of solids. It is evident that, if the applied stress or experimental time (strain rate) is below a critical value, i.e. $\dot{\gamma}\eta_N \frac{V}{3kT_g} < 1$, the “glass” systems show the liquid behaviour and the rheology is dominated by thermally activated Newtonian flow in **Fig. 2d**. However, when $\dot{\gamma}\eta_N \frac{V}{3kT_g} > 1$, the systems become solid-like and the rheology is mainly controlled by stress-driven cooperative shear. Conventionally, this yielding or shear thinning process is considered as the onset of time-independent elastic-plastic flow in glassy materials or unjamming in granular materials as the transient plastic flow is readily noticed. In other words, the universal scaling law reveals a mechanistic transition from thermally activated Newtonian flow to stress-driven cooperative shear which takes place when

$$\dot{\gamma}\eta_N \frac{V}{3kT_g} = 1 \quad (3)$$

Therefore, the transition between liquid and glass essentially depends on four parameters: molar volume V or density; temperature, T ; experimental or observation time, $\dot{\gamma}$ or t_{obs} ; and stress, τ . In principle, the transition can be defined by one of the

four variables and described by a three dimensional (3D) contoured surface in temperature-stress-volume, temperature-stress-time, temperature-time-volume, or time-volume-stress phase spaces. For example, in a typical case of time being the critical variable^{23,37-39}, the transition can be presented on a 3D contoured surface in the temperature-stress-volume space with three scaled variables: kT/U_0 , τ/τ_0 and V/V_0 as the axes (**Fig. 3a**). Here, $U_0=3kT_g$ is the thermal energy required for glass transition at zero stress and maximum density³⁵, τ_0 is the critical strength at 0 K and maximum density, and V_0 is the molar volume at 0 K and at zero stress. The transition boundary can be determined by critical-like equations where the three scaled variables are correlated^{38,40} (*see Supplementary Information*). Experimental data of the transition for metallic glasses, plotted as red solid spheres, locate at the transition boundary^{9,41}, together with the literature data for a granular system under constant driving force or tapping as dark grey spheres⁴² and attractive particles with $U_0 \approx 20kT$ as navy spheres³⁸ in **Fig. 3a**. The transition points from the master curves in **Fig. 2d** are also plotted in **Fig. 3a**. The glass systems are in an equilibrium and reversible state underneath the contoured boundary, but become off-equilibrium and irreversible above the boundary.

In practice, one of the three thermodynamic variables often keeps constant or approximately unchanged during experiments and thereby the transition can be determined by a planar cut of the 3D contour. For examples, under constant driving force, the transition boundary in the granular system from reversible to irreversible regimes by jamming and unjamming can be plotted as a contour curve in the 2D domain of temperature (or tapping amplitude) and molar volume (or density) in **Fig. 3b**. For the

attractive particles at a constant temperature, the transition boundary is a contour curve in V/V_0 or $(V/V_0)^{\lambda_v}$ and τ/τ_0 domain in **Fig. 3c**. The exponential dependence is related to the formation of clusters in attractive particles, in which case the density of a fractal aggregate decreases as the cluster grows³⁸. In the case of metallic glasses, the density change is negligible and the transition is well presented in the temperature-stress domain in **Fig. 3d**. For our broadband stress relaxation measurements, the temperature and volume are nearly constant, thus the rheological behaviour is degenerated to the correlation between time (strain rate) and shear stress, and the transition can be conveniently defined by either correlated time (strain rate) or stress^{23,35}.

Liu and Nagel³⁷ have proposed a famous conjecture that the dynamic transitions in a variety of disordered systems, such as jamming-unjamming transition in granular materials and foams and liquid-to-glass transition in glass-forming materials, can be brought together under one rubric and unified by a 3D jamming phase diagram parameterized by thermodynamic variables of temperature, density (volume) and force. In the past decade, this hypothesis has been partially confirmed by computer simulations and experiments in granular and glass systems^{23,38,39,43,44}. However, the comprehensive validation has not been achieved. It is intriguing to note that our universal scaling law, derived from the dynamic responses of a broad range of “glass” systems, provides solid theoretical confirmation on the hypothesis. The resulting phase diagram in the temperature-stress-volume space (**Fig. 3**), identical to the concept of jamming phase diagram, can quantitatively represents the experimental observations on

temperature- and volume-controlled jamming transition of a granular system with constant driving force, stress- and volume-controlled jamming transition in attractive particles, and temperature- and stress-controlled glass transitions in glass materials. Importantly, the unified phase diagram from the universal scaling law unveils the dynamic nature of “glass” systems in the framework of liquid dynamics, i.e. the jamming and glass transitions occur in trajectory space (space-time) rather than in configuration space and, therefore, are controlled by thermodynamic variables of stress (pressure), volume (density) and temperature that drive the systems out of equilibrium⁴⁵. In fact, the “glass” systems are ergodic when they are in the equilibrium Newtonian flow region. When the system is out of equilibrium above the phase boundary, it is nonergodic and the motions of the constituent particles become correlated throughout the observation time. The boundary for the transition where the ergodic and nonergodic phases are separated by a critical temporal variable can thus be described by a contoured surface of three thermodynamic parameters: stress (pressure), volume (density) and temperature by the universal scaling law and the dynamic (jamming) phase diagram.

Besides the scientific importance of the universal scaling law in unveiling the nature of “glasses” and in describing the dynamic transitions of “glass” systems, the scaling law also provides importance guidance for designing and employing “glass” materials for practical applications. For example, the equal role of temperature and stress in glass transition directs the alloy design of high-temperature metallic glasses by considering strong and refractory elements⁴⁶, and warrants attention on the thermal and

mechanical stability of glasses as a force-bearing component serving at the temperatures even below T_g that is conventionally determined by differential scanning calorimetry at zero force. For granular materials, the universal scaling law may bring new insights and attention on the possible effect of temperature, in addition to the known pressure and density, on landslides and riverbank collapses by soil liquefaction⁴⁷.

In summary, the broadband dynamic response of MGs, together with a wide variety of other “glass” systems, can be unified by a universal scaling law within the framework of fluid dynamics. The scaling law provides comprehensive validation of the conjecture of jamming phase diagram and demonstrates that the dynamic transitions of disorder systems can be described by the conversion between equilibrium Newtonian liquids and off-equilibrium elastic-plastic solids. This work uncovers the liquid nature of glasses and offers quantitative description on the dynamic transitions of “glass” systems by thermodynamic variables of temperature, volume and stress in trajectory space.

References

- 1 Anderson, P. W. Through the Glass Lightly. *Science* **267**, 1615-1616 (1995).
- 2 Kennedy, D. & Norman, C. What Don't We Know? *Science* **309**, 75-75 (2005).
- 3 Langer, J. The Mysterious Glass Transition. *Physics Today - PHYS TODAY* **60** (2007).

- 4 Ediger, M. D. & Harrowell, P. Perspective: Supercooled liquids and glasses. *The Journal of Chemical Physics* **137**, 080901 (2012).
- 5 Frost, H. J., Ashby, Michael F. *Deformation-mechanisms maps: the plasticity and creep of metals and ceramics*. 165 (Pergamon Press, 1982).
- 6 Chang, K. *The Nature of Glass Remains Anything but Clear*, The New York Times, <<https://www.nytimes.com/2008/07/29/science/29glass.html>> (July 29, 2008).
- 7 Argon, A. S. Plastic-deformation in metallic glasses. *Acta Metall.* **27**, 47-58 (1979).
- 8 Spaepen, F. A microscopic mechanism for steady-state inhomogeneous flow in metallic glasses. *Acta Metall.* **25**, 407-415 (1977).
- 9 Johnson, W. L. & Samwer, K. A universal criterion for plastic yielding of metallic glasses with a $(T/T_g)^{2/3}$ temperature dependence. *Phys. Rev. Lett.* **95**, 195501 (2005).
- 10 Chen, M. W. Mechanical behavior of metallic glasses: Microscopic understanding of strength and ductility. *Ann. Rev. Mater. Res.* **38**, 445-469 (2008).
- 11 Falk, M. L., Langer, J. S. & Pechenik, L. Thermal effects in the shear-transformation-zone theory of amorphous plasticity: Comparisons to metallic glass data. *Phys. Rev. E* **70**, 011507 (2004).

- 12 Hufnagel, T. C., Schuh, C. A. & Falk, M. L. Deformation of metallic glasses: Recent developments in theory, simulations, and experiments. *Acta Mater.* **109**, 375-393 (2016).
- 13 Ju, J. D., Jang, D., Nwankpa, A. & Atzmon, M. An atomically quantized hierarchy of shear transformation zones in a metallic glass. *J. Appl. Phys.* **109**, 053522 (2011).
- 14 Pan, D., Inoue, A., Sakurai, T. & Chen, M. W. Experimental characterization of shear transformation zones for plastic flow of bulk metallic glasses. *Proc. Natl. Acad. Sci. U.S.A.* **105**, 14769-14772 (2008).
- 15 Puthoff, J. B., Jakes, J. E., Cao, H. & Stone, D. S. Investigation of thermally activated deformation in amorphous PMMA and Zr-Cu-Al bulk metallic glasses with broadband nanoindentation creep. *J. Mater. Res.* **24**, 1279-1290 (2009).
- 16 Schuh, C. A., Hufnagel, T. C. & Ramamurty, U. Mechanical behavior of amorphous alloys. *Acta Mater.* **55**, 4067-4109 (2007).
- 17 Liu, Y. H. *et al.* Deposition of multicomponent metallic glass films by single-target magnetron sputtering. *Intermetallics* **21**, 105-114 (2012).
- 18 Pietanza, L. D., Colonna, G., Longo, S. & Capitelli, M. Electron and phonon relaxation in metal films perturbed by a femtosecond laser pulse. *Appl. Phys. A* **79**, 1047-1050 (2004).

- 19 Qiao, J. C. & Pelletier, J. M. Dynamic mechanical analysis in La-based bulk metallic glasses: Secondary (β) and main (α) relaxations. *J. Appl. Phys.* **112**, 083528 (2012).
- 20 Angell, C. A. Perspective on the glass transition. *J. Phys. Chem. Solids* **49**, 863-871 (1988).
- 21 Ngai, K. L. *Relaxation and Diffusion in Complex Systems*. (Springer, 2011).
- 22 Lu, J., Ravichandran, G. & Johnson, W. L. Deformation behavior of the $Zr_{41.2}Ti_{13.8}Cu_{12.5}Ni_{10}Be_{22.5}$ bulk metallic glass over a wide range of strain-rates and temperatures. *Acta Mater.* **51**, 3429-3443 (2003).
- 23 Guan, P., Chen, M. & Egami, T. Stress-Temperature Scaling for Steady-State Flow in Metallic Glasses. *Phys. Rev. Lett.* **104**, 205701 (2010).
- 24 Park, K.-W., Lee, C.-M., Kim, H.-J., Lee, J.-H. & Lee, J.-C. A methodology of enhancing the plasticity of amorphous alloys: Elastostatic compression at room temperature. *Mater. Sci. Eng., A* **499**, 529-533 (2009).
- 25 Song, S. X. & Nieh, T. G. Direct measurements of shear band propagation in metallic glasses – An overview. *Intermetallics* **19**, 1968-1977 (2011).
- 26 Yoo, B.-G. *et al.* Increased time-dependent room temperature plasticity in metallic glass nanopillars and its size-dependency. *Int. J. Plast.* **37**, 108-118 (2012).
- 27 Brückner, R. & Yue, Y. Non-Newtonian flow behaviour of glass melts as a consequence of viscoelasticity and anisotropic flow. *J. Non-Cryst. Solids* **175**, 118-128 (1994).

- 28 Köpplmayr, T. *et al.* A novel online rheometer for elongational viscosity measurement of polymer melts. *Polym. Test.* **50**, 208-215 (2016).
- 29 Malkin, A. Y. Non-Newtonian viscosity in steady-state shear flows. *J. Non-Newtonian Fluid Mech.* **192**, 48-65 (2013).
- 30 Roland, C. M. *Chapter 6 - Rheological Behavior and Processing of Unvulcanized Rubber.* Fourth Edition edn, (Academic Press, 2013).
- 31 Mackley, M. R. *et al.* The observation and evaluation of extensional filament deformation and breakup profiles for Non Newtonian fluids using a high strain rate double piston apparatus. *J. Non-Newtonian Fluid Mech.* **239**, 13-27 (2017).
- 32 Olsson, P. & Teitel, S. Critical Scaling of Shear Viscosity at the Jamming Transition. *Physical Review Letters* **99**, 178001 (2007).
- 33 Jeong, S. W., Locat, J., Leroueil, S. & Malet, J.-P. Rheological properties of fine-grained sediment: the roles of texture and mineralogy. *Canadian Geotechnical Journal* **47**, 1085-1100 (2010).
- 34 Tennenbaum, M., Liu, Z., Hu, D. & Fernandez-Nieves, A. Mechanics of fire ant aggregations. *Nat. Mater.* **15**, 54-59 (2016).
- 35 Liu, Y. H. *et al.* Thermodynamic origins of shear band formation and the universal scaling law of metallic glass strength. *Phys. Rev. Lett.* **103**, 065504 (2009).
- 36 Bird, R. B., Dai, G. C. & Yarusso, B. J. The Rheology and Flow of Viscoplastic Materials. *Reviews in Chemical Engineering* **1**, 1 (1983).

- 37 Liu, A. J. & Nagel, S. R. Nonlinear dynamics: Jamming is not just cool any more. *Nature* **396**, 21-22 (1998).
- 38 Trappe, V., Prasad, V., Cipelletti, L., Segre, P. N. & Weitz, D. A. Jamming phase diagram for attractive particles. *Nature* **411**, 772 (2001).
- 39 Ciamarra, M. P., Pastore, R., Nicodemi, M. & Coniglio, A. Jamming phase diagram for frictional particles. *Physical Review E* **84**, 041308 (2011).
- 40 Makse, H. A., Johnson, D. L. & Schwartz, L. M. Packing of Compressible Granular Materials. *Physical Review Letters* **84**, 4160-4163 (2000).
- 41 He, Y., Schwarz, R. B. & Mandrus, D. G. Thermal expansion of bulk amorphous $Zr_{41.2}Ti_{13.8}Cu_{12.5}Ni_{10}Be_{22.5}$ alloy. *J. Mater. Res.* **11**, 1836-1841 (2011).
- 42 Coniglio, A., de Candia, A., Fierro, A., Nicodemi, M. & Tarzia, M. Statistical mechanics approach to the jamming transition in granular materials. *Physica A: Statistical Mechanics and its Applications* **344**, 431-439 (2004).
- 43 Bi, D., Zhang, J., Chakraborty, B. & Behringer, R. P. Jamming by shear. *Nature* **480**, 355-358 (2011).
- 44 Kumar, A. & Wu, J. Jamming phase diagram of colloidal dispersions by molecular dynamics simulations. *Applied Physics Letters* **84**, 4565-4567 (2004).
- 45 Hedges, L. O., Jack, R. L., Garrahan, J. P. & Chandler, D. Dynamic order-disorder in atomistic models of structural glass formers. *Science* **323**, 1309-1313 (2009).

- 46 Li, M.-X. *et al.* High-temperature bulk metallic glasses developed by combinatorial methods. *Nature* **569**, 99-103 (2019).
- 47 Lakeland, D. L., Rechenmacher, A. & Ghanem, R. Towards a complete model of soil liquefaction: the importance of fluid flow and grain motion. *Proceedings of the Royal Society A: Mathematical, Physical and Engineering Sciences* **470**, 20130453 (2014).
- 48 Yang, R. Q., Fan, J. T., Li, S. X. & Zhang, Z. F. Fracture behavior of Zr₅₅Cu₃₀Al₁₀Ni₅ bulk metallic glass under quasi-static and dynamic compression. *J. Mater. Res.* **23**, 1744-1750 (2008).
- 49 Oliver, W. C. & Pharr, G. M. An Improved Technique for Determining Hardness and Elastic-Modulus Using Load and Displacement Sensing Indentation Experiments. *Journal of Materials Research* **7**, 1564-1583 (1992).
- 50 Poisl, W. H., Oliver, W. C. & Fabes, B. D. The Relationship between Indentation and Uniaxial Creep in Amorphous Selenium. *J. Mater. Res.* **10**, 2024-2032 (1995).
- 51 Weihs, T. P., Hong, S., Bravman, J. C. & Nix, W. D. Mechanical deflection of cantilever microbeams: A new technique for testing the mechanical properties of thin films. *J. Mater. Res.* **3**, 931-942 (1988).

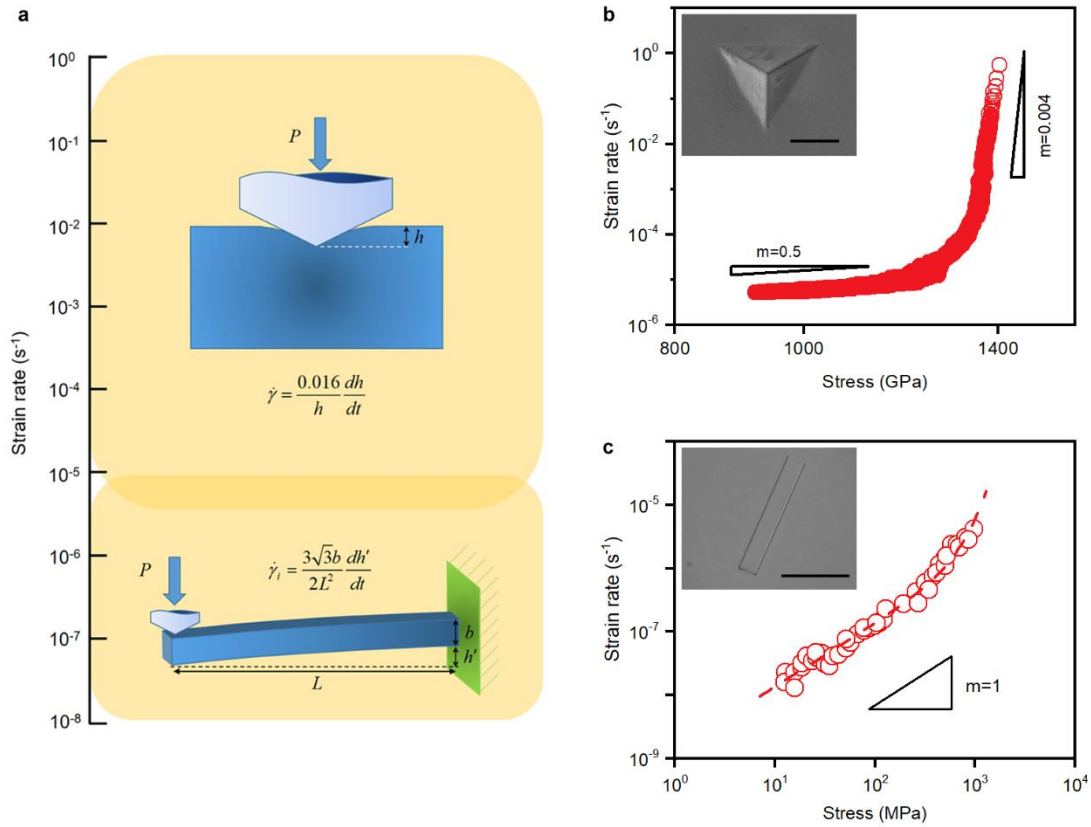


Fig. 1. Broadband relaxation measurements of a $Zr_{55}Cu_{30}Ni_5Al_{10}$ Glass. a, Schematic drawing of broadband stress relaxation experiments by using nanoindentation (above) and cantilever bending (bottom) tests with a total measurable strain rate range from 10^{-8} to $10^0 s^{-1}$. **b, c**, Shear strain rate as a function of shear stress calculated from nanoindentation relaxation measurements (**b**) and from cantilever bending relaxation measurements (**c**). SEM images of an indent after a nanoindentation relaxation test at 10 mN for 2000 s with a scale bar of 1 μm and a typical cantilever with a scale bar of 100 μm are inserted respectively. Rate sensitivity (m) of 1, 0.5 and 0.004 is plotted as triangle slope for eye guide.

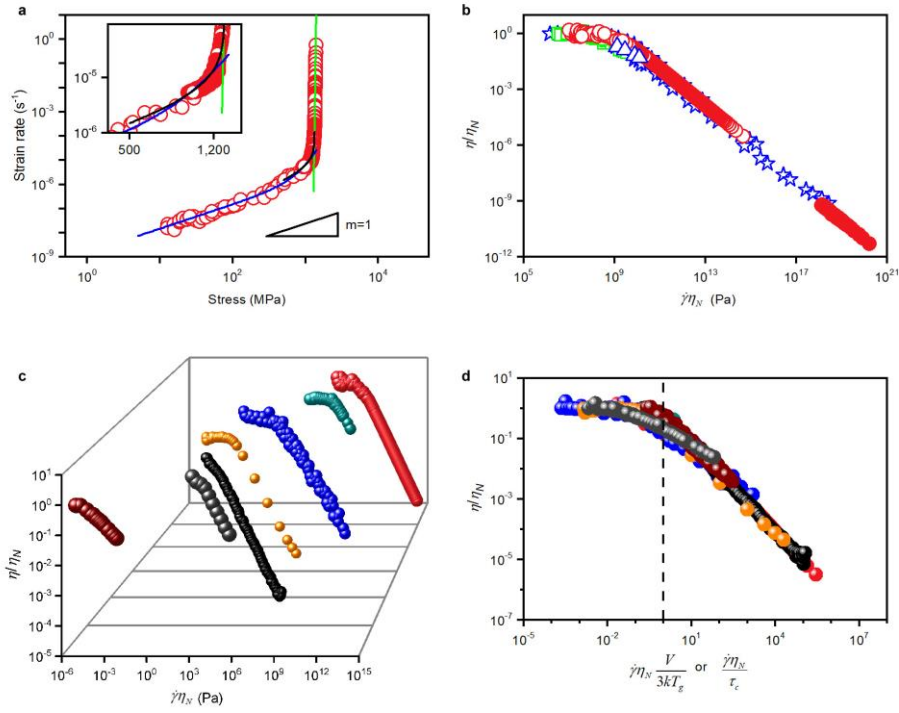


Fig. 2. Strain rate-stress behaviour and universal scaling law of glass rheology. a,

The plot of logarithmic shear strain rate as a function of logarithmic shear stress for the $Zr_{55}Cu_{30}Ni_5Al_{10}$ glass under nanoindentation and cantilever bending at room temperature. Rate sensitivity (m) of 1 is plotted as triangle slope for eye guide. The inset is the enlarged view of the transition segment together with the fitting curves based on the transition state theory (blue line), cooperative shear model (green line) and Kohlrausch relaxation equation (black line). **b,** Normalized viscosity as a function of scaled strain rate by Newtonian viscosity from the broadband relaxation measurements at room temperature (red open circles), creep data from compression at room temperature (blue open triangles)^{24,26} and 613 – 683 K in Vitreloy 1 glass (green open squares)²² together with molecular dynamic simulation results in a Cu-Zr glass (blue pentacle)²³ and viscosity measured for propagating shear band in a

Zr-BMG at room temperature (solid red circles) ²⁵. **c**, Normalized viscosity as a function of scaled strain-rate by Newtonian viscosity from various glassy materials. Metallic glasses data is plotted as red balls. Silicate glass non-Newtonian flow data is plotted as dark cyan balls ²⁷. Viscosity data in polyethylene²⁹, polypropylene²⁸, and polybutadiene rubber ³⁰ are plotted as blue balls. The ant aggregation viscous data is plotted as dark balls ³⁴. Mayonnaise non-newtonian flow data is plotted as orange balls ³¹. Granular ³² and soil ³³ data are plotted as dark grey and wine balls. **d**, Normalized viscosity as a function of dimensionless quantities as $\dot{\gamma}\eta_N \frac{V}{3kT_g}$ or $\frac{\gamma\eta_N}{\tau_c}$ in various glassy materials and the dashed line at $\dot{\gamma}\eta_N \frac{V}{3kT_g}=1$ is for guidance.

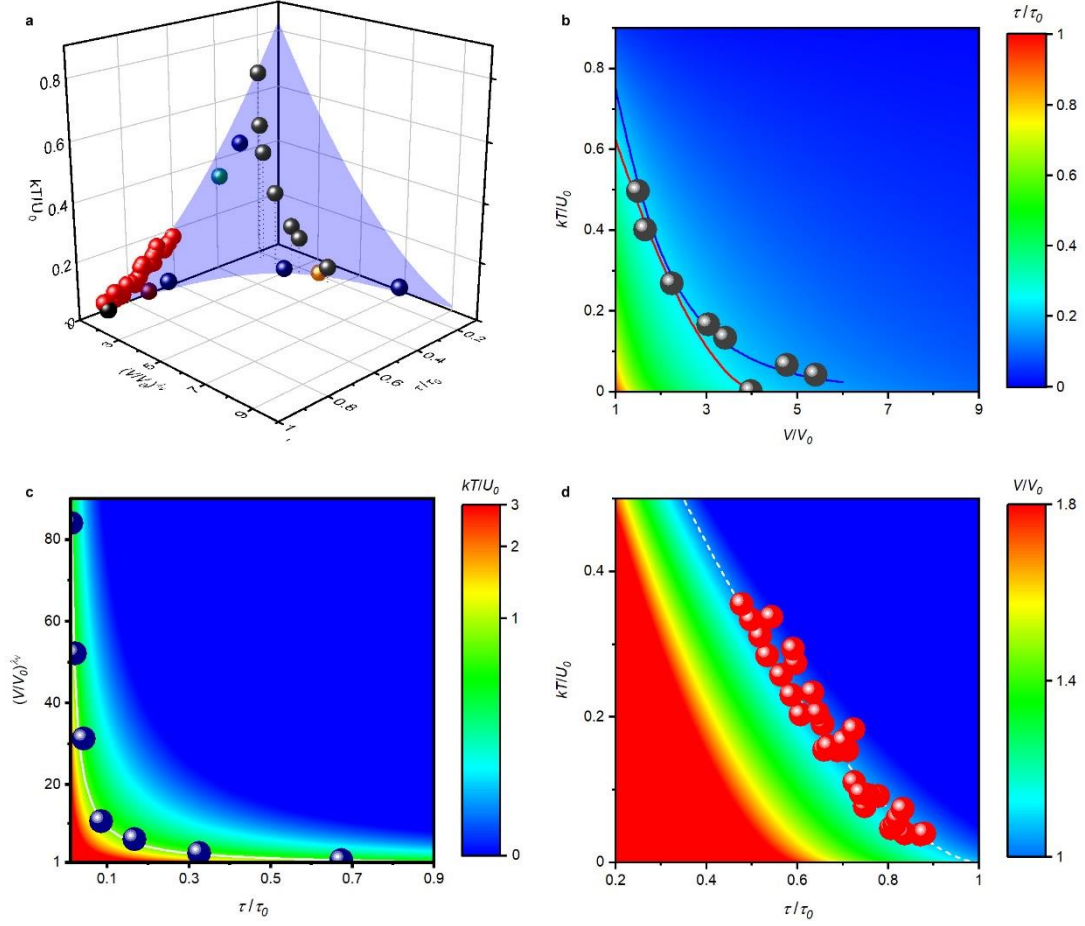


Fig. 3: Dynamic transition phase diagram based on the universal law derived from the broadband relaxation measurements. a, Perspective view of the transition boundary diagram plotted as light blue surface with normalized stress τ/τ_0 , normalized molar volume $(V/V_0)^{\lambda_v}$, and reduced temperature kT/U_0 following **Equations (3)** and **(S15)** when $\lambda_v = 1$. The temperature dependence on τ/τ_0 and V/V_0 in various metallic glasses⁹ and this study is plotted as red balls which coincide on the boundary surface at the MG region. The jamming transition boundary in attractive particles from literature at $U_0 \approx 20kT$ ³⁸ and granular materials⁴² are plotted as navy balls and dark grey balls respectively. The transition points of the glassy materials from **Fig. 2c** are also plotted. **b**, Phase diagram is plotted of two control parameters: kT/U_0

and V/V_0 in a granular system with constant driving force. **c**, Two-dimensional boundary plot of τ/τ_0 as a function of V/V_0 at $U_0 \approx 20kT$ for attractive polystyrene particles, the molar volume is normalized with $(V/V_0)^{\lambda_v}$ with $\lambda_v = 3.2$. **d**, Two-dimensional boundary plot of τ/τ_0 as a function of kT/U_0 at constant V/V_0 for metallic glasses. See **Supplementary Information** for details on curve fitting.

Methods

Sample preparation

$Zr_{55}Cu_{30}Al_{10}Ni_5$ (at %) metallic glass is selected as a model system for the broadband stress relaxation experiments. Glassy films with 5 μm thickness were prepared by a single-target magnetron sputtering method using a multicomponent $Zr_{55}Cu_{30}Al_{10}Ni_5$ alloy as the target¹⁷. The deposition was conducted with a radio frequency power of 100W at room temperature. The base pressure was 3×10^{-4} Pa and the working pressure was tuned to 0.3 Pa with high purity argon gas. Si (100) wafers with diameter of 50 mm were used as substrates. Freestanding film samples were obtained by dissolving the silicon substrate in NaOH-water solution. The glass transition temperature of the film was measured to be 695 K by DSC with a PerkinElmer 8500 instrument under a purified argon atmosphere at a heating rate of 20 K/min, consistent with that of the $Zr_{55}Cu_{30}Al_{10}Ni_5$ bulk samples and previous reports^{17,48}. The 5 μm thick, 25 μm wide, and 200 μm long cantilevers were machined by focused ion beam (FIB) in a dual beam SEM (FEI Versa 3D) system with 30 kV accelerating voltage and 0.5 nA Ga^+ ion current. Larger cantilevers of 30 μm thick, 70 μm wide and 700 μm long are prepared by machining $Zr_{55}Cu_{30}Ni_5Al_{10}$ ribbons using a low speed saw. Ribbon samples were produced by melt-spinning the $Zr_{55}Cu_{30}Al_{10}Ni_5$ alloy on a copper wheel at a rotation speed of about $420 \text{ rad} \cdot \text{s}^{-1}$ in argon atmosphere.

Structural characterization

The microstructure of the as-prepared thin films was characterized by transmission electron microscopy (TEM). The TEM samples were prepared by ion milling using a Gatan PIPS-II ion miller equipped with liquid nitrogen cooling holder. TEM experiments were conducted by a JOEL ARM200F TEM operating at an acceleration voltage of 200 kV. The selected area electron diffraction pattern of the $Zr_{55}Cu_{30}Al_{10}Ni_5$ thin films shows diffusive amorphous halos in **Extended Data Fig. 4a**, demonstrating the amorphous nature of the samples. The high-resolution TEM image of **Extended Data Fig. 4b** further verified that visible crystallites could not be

found and the alloy used in the stress relaxation experiments has a fully amorphous structure. The morphology and size of the cantilever samples and the indents of nanoindentation experiments were inspected by scanning electron microscopy (SEM) in a FEI Versa 3D SEM with 5 kV accelerating voltage.

Broadband nanoindentation relaxation experiments

The elastic modulus (E) and hardness (H) of the metallic glass is determined to be 121.5 GPa and 6.7 GPa at room temperature (295 K), following Oliver-Pharr method⁴⁹, by a nano-indentation instrument (Hysitron Triboindenter, Minneapolis, MN) equipped with a Berkovich indenter at the peak force of 10 mN and the loading/unloading rate of 0.2 mN/s. The nanoindentation relaxation tests were performed by applying the load to 10 mN in 0.05 seconds, holding at 10 mN for up to 200 seconds for quasi-static relaxation measurements and up to 2000 seconds for dynamic relaxation measurements, and then unloading in 0.05 seconds. Indentation depths were all within 300 nm, much smaller than 10% of the film thickness, avoiding possible influence from substrates. The load and depth were recorded at data acquisition rate up to 2000 points per second for relaxation tests.

In order to obtain reliable and accurate relaxation data, the following procedures are followed. The area function of the probe is carefully calibrated on fused quartz to get area function constants C_1 to C_6 as listed in **Extended Data Table 3** by equation (S1)⁴⁹.

$$A(h) = \sum_{i=1}^6 C_i \cdot (h - 0.75 P_{\max} / S)^{4/2^i} \quad (\text{S1})$$

where $A(h)$ is the contact area as a function of indentation depth (h), P_{\max} is the peak force, and S is the contact stiffness measured from unloading segments. The nanoindentation relaxation results in this study were obtained at depths larger than 200 nm to avoid the tip radius effect which is evident at depths lower than 30 nm. The geometry of the indents for 2000 seconds relaxation tests is also characterized by SEM and is shown in **Fig. 1b**.

In order to minimize the thermal drift effect from the nanoindentation relaxation measurements, all tests were performed at least 2 hours after samples were placed in the instrument chamber for sufficient system stabilization. The typical thermal drift rate of the system was calibrated by a fused quartz sample with 1 μN contact force in every 40 seconds and was plotted in **Extended Data Fig. 5a**. The thermal drift rates are all within $\pm 0.02 \text{ nm}\cdot\text{s}^{-1}$ in this study. Before each test, the probe is engaged onto the sample surface and waits 300 seconds for stage motor and piezo to settle. After that, the thermal drift was monitored for 100 seconds with 1 μN contact force before each test and with 5% peak force after each test. The average thermal drift rate was calculated and subtracted from each relaxation measurement. Typical quasi-static nanoindentation relaxation data with constant 10 mN force is plotted in **Extended Data Fig. 5b**. The measured strain rates are all above the thermal drift rate during 200 s relaxation. Thus, standard quasi-static nanoindentation relaxation measurement is reliable as long as 200 seconds, beyond which the thermal drift may interfere the low rate measurements. Additional indentation relaxation at lower stress and lower strain-rate was measured by loading to 10 mN and then monitoring the dynamic contact stiffness with 0.2 mN load amplitude and 200 Hz frequency for as long as 2000 seconds. The indentation depth was estimated from the measured dynamic contact stiffness which had negligible thermal drift effect because the high dynamic loading frequency is comparable to the low drift rate. The measured contact stiffness (S) was used to estimate the indentation depths (h) following **Equation (S2)** ⁴⁹.

$$E = \frac{S\sqrt{\pi}}{2\sqrt{A(h)}} \quad (\text{S2})$$

where E is the Young's modulus (121.5 GPa) and $A(h)$ is the area function **equation (S1)**, both of which are assumed to be constants during the test. Since the displacement amplitude is around 1 nm within a period of 1/200 s, the dynamic displacement rate is above 200 nm/s, which is much higher than the thermal drift rate of 0.02 nm/s. Thus, the thermal drift can be ignored and the measured contact stiffness and calculated indentation depth by **equations (S1)** and **(S2)** are plotted as a function

of relaxation time in **Extended Data Fig. 5c** and **d** respectively. It is noted that dynamic tests cannot measure the highest stress and/or strain rate region at the early stage of relaxation, for example 0 – 20 s, therefore the static (0 – 200 s, **Extended Data Fig. 5b**) and dynamic (20 – 2000s, **Extended Data Fig. 5d**) relaxation results are plotted together in **Extended Data Fig. 5e**, which overlap well in the time range from 20 s to 200 s and form a continuous line.

With the nanoindentation measurements, shear-strain rate ($\dot{\gamma}$) beneath the indenter is derived from the displacement rate (dh/dt) and depth (h) through an equation⁵⁰:

$$\dot{\gamma} = 0.16 \frac{1}{h} \frac{dh}{dt} \quad (\text{S3})$$

The hardness of the $\text{Zr}_{55}\text{Cu}_{30}\text{Al}_{10}\text{Ni}_5$ metallic glass was measured to be 6.7 GPa at room temperature which is about 3.5 times of the compression strength of 1.9 GPa⁴⁸. Since the pure shear stress is approximately $\sqrt{3}$ times lower than the uniaxial yield stress under the monotonic loading conditions according to von Mises yield criterion, the hardness/shear strength ratio is approximately $3.5\sqrt{3}$. Thus, the nominal shear stress (τ) can be estimated from indentation depth (h) and load (P) by:

$$\tau = \frac{\sigma}{\sqrt{3}} = \frac{P}{3.5\sqrt{3}A(h)}, \quad (\text{S4})$$

where σ is the normal stress, $A(h)$ is the area function of the indenter which has been carefully calibrated before and after the relaxation tests. With the data of depth versus time in **Extended Data Fig. 5e** at constant force of 10 mN, the nominal shear stress and shear strain-rate as a function of time can be derived and are plotted in **Extended Data Fig. 5f**. The nominal shear stress beneath the indenter decreases from 1402.6 MPa \pm 5 MPa to 1057.1 MPa \pm 35 MPa during the relaxation from 0 s to 2000 s. Accordingly, the strain rate in relaxation testing covers more than four orders of magnitude from 0.56 s⁻¹ to 5.3 \times 10⁻⁶ s⁻¹ (**Extended Data Fig. 5f**). The estimated shear stress is plotted as the function of shear strain rate in **Fig. 1b**, in which the shear stress has a linear log-log relation with shear strain rate in the high stress region above 1350

MPa. The slope of the linear portion, or the strain-rate sensitivity ($m = \partial \ln \tau / \partial \ln \dot{\gamma}$), is calculated to be 0.004 ± 0.001 , consistent with that of rate-jump indentation measurements¹⁴. The strain-rate sensitivity gradually increases to ~ 0.5 when the strain rate decreases to $\sim 3 \times 10^{-5} \text{ s}^{-1}$ and stresses is below 1100 MPa. For the broadband nanoindentation experiments, it approaches the rate limit when the relaxation extends longer than 2000 s with a resulting strain rate of $5.3 \times 10^{-6} \text{ s}^{-1}$. Beyond the time limit, the relaxation measurements will be obviously interfered by lateral thermal drift. To overcome the technical limitation, we employed a nanoindentation based cantilever bending method⁵¹ to detect the flow behaviour of metallic glasses in a low strain rate range from 10^{-8} to 10^{-6} s^{-1} .

Cantilever relaxation experiments

Typical cantilevers with sizes are shown in **Extended Data Fig. 6a** and **b**. A conical indenter with $1.5 \text{ }\mu\text{m}$ tip radius was loaded on the cantilever with a constant force of 1.0, 1.5, 2, 2.5, 3, 3.5, 4.5, 6, 8, 10 mN using a Hysitron Triboindenter. The distance between the clamp and indenter tip contact point was $400 \text{ }\mu\text{m}$ for $30 \times 70 \times 700 \text{ }\mu\text{m}^3$ cantilevers and $50 \text{ }\mu\text{m}$ for $5 \times 25 \times 200 \text{ }\mu\text{m}^3$ cantilevers. The indenter displacement was measured during the constant force relaxation for 1000 seconds, and anelastic recovery was also monitored for 1000 seconds with $1 \text{ }\mu\text{N}$ force. Thermal drift was measured with $1 \text{ }\mu\text{N}$ contact force for 200 seconds before each test and was subtracted. Indenter displacements, or cantilever deflection displacements (h'), as a function of time during relaxation tests are plotted in **Extended Data Fig. 6c** and **d** for $5 \text{ }\mu\text{m}$ and $30 \text{ }\mu\text{m}$ thick cantilevers, respectively. The corresponding shear stresses (τ) and instantaneous shear strains (γ_i) at the pivot point of cantilevers are calculated by:

$$\tau = \frac{6PL}{\sqrt{3}wb^2} \quad \text{and} \quad \gamma_i = \frac{3\sqrt{3}bh'}{2L^2}, \quad (\text{S5})$$

where P is the load, L is the distance between the clamp and indenter tip contact point, b is the sample thickness, w is the width of the cantilever and h' is the bending

displacement⁵¹. Calculated shear strains at the pivot point under constant loading forces of 1 to 10 mN in the cantilevers are plotted as the function of time in **Extended Data Fig. 6c** and **d**. Relaxation process is readily observed in the constant force segment and anelastic recovery takes place in the unloading segment. The permanent strain is obtained by subtracting the anelastic strain (γ_a) from the total relaxation strain (γ_t) to estimate shear strain rates, $\dot{\gamma} = (\gamma_t - \gamma_a) / \Delta t$, at various stresses for a duration of $\Delta t = 1000$ s and are plotted with shear stress in **Fig. 1c**. The measured strain rates cover the range from 10^{-8} to 10^{-6} s⁻¹. The strain rate sensitivity (m) keeps increasing with the decrease of strain rate and reaches a constant value of ~ 1.0 when the strain rate is lower than 10^{-7} s⁻¹ in **Fig. 1c**.

Acknowledgments:

Funding: Sponsored by National Natural Science Foundation of China (Grant No. 51821001). M.C. thanks the support from Whiting School of Engineering, Johns Hopkins University and National Science Foundation (NSF PD 09-1771).

Author contributions: S.X.S designed and performed the broadband stress relaxation experiments and data process, F.Z. prepared the metallic glass samples and conducted microstructure characterization, S.X.S and M.W.C analysed the data, developed the models and wrote the paper. M.W.C conceived and supervised the project.

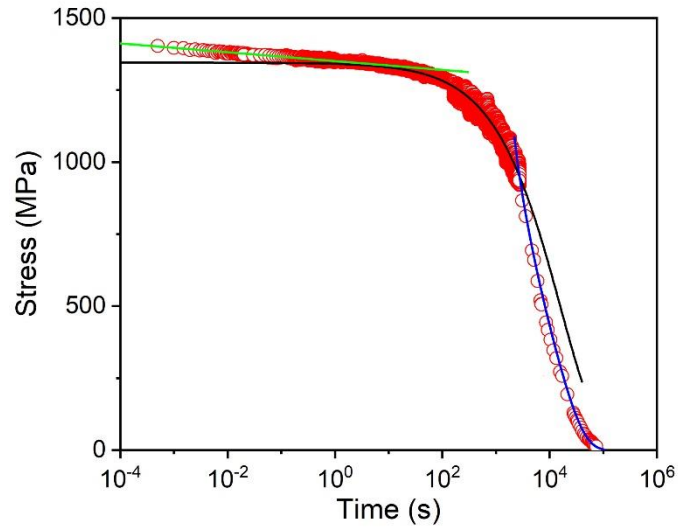
Competing financial interests: The authors declare no competing financial interests.

Additional Information: Supplementary Information is available for this paper.

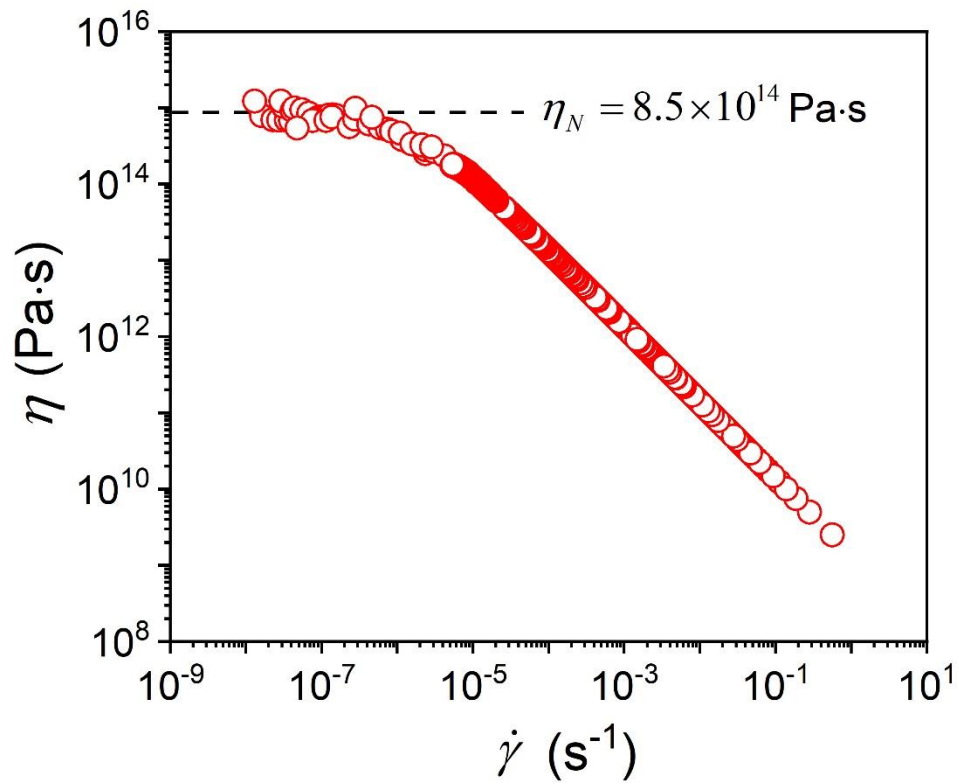
Data availability

The data that support the plots and other analysis in this work are available upon request.

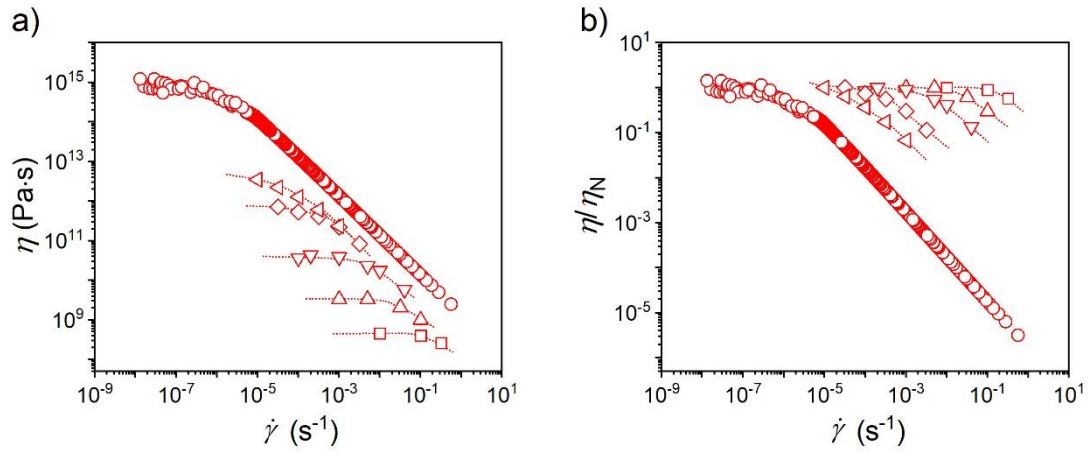
Extended Data Figures and Tables



Extended Data Fig. 1. Shear stress as a function of experimental time measured by the broadband nanoindentation relaxation experiments at room temperature (295 K). Experimental results from this study are plotted as open red circles. The green line is CSM fitting with equation (S11), the dark line is Kohlrausch function fitting with equation: $\tau = \tau_0 \cdot \exp\left[-\left(t/t_a\right)^\beta\right]$, using $t_a = 1.6 \times 10^4$ s and $\beta = 0.6$, and the blue line is the Argon's fitting with equation (S9).

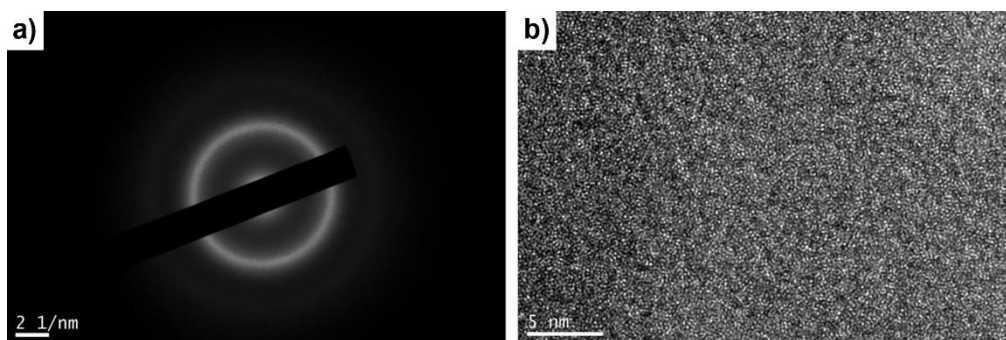


Extended Data Fig. 2. The viscosity as a function of shear strain rate of the **Zr₅₅Cu₃₀Al₁₀Ni₅** metallic glass at 295 K derived from Fig. 2a. The Newtonian viscosity is marked as a dashed line.

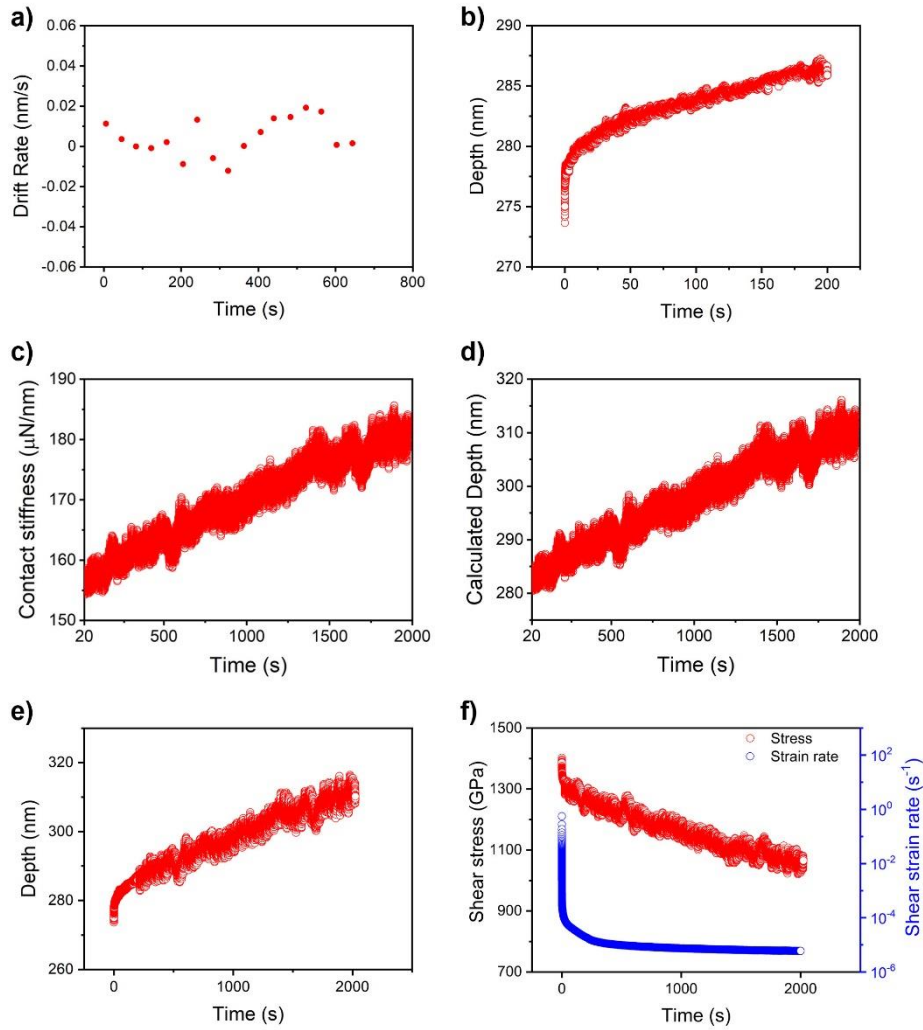


Extended Data Fig. 3. Compare the current data at room temperature with literature data of other Zr-based metallic glasses achieved at high temperatures.

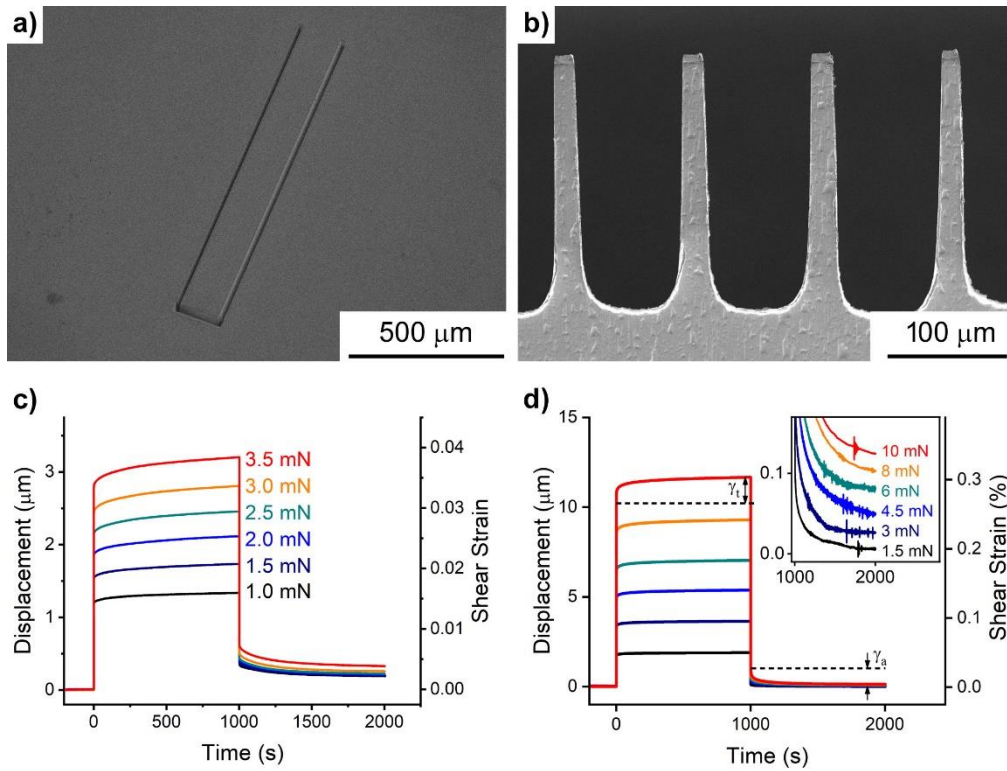
a, Viscosity data as a function of shear strain rate. **b**, Viscosity data normalized by Newtonian viscosity and plotted as a function of shear strain rate. Experimental results from this study are plotted as open red circles. The literature data of Vitreloy 1 MG²² are plotted as \square (683K), \triangle (663 K), ∇ (643 K), \diamond (623 K), and \blacktriangleleft (613 K). Dotted lines provide guidance for each temperature.



Extended Data Fig. 4. Transmission electron microscopic images of the $\text{Zr}_{55}\text{Cu}_{30}\text{Al}_{10}\text{Ni}_5$ metallic glass. a, Selected area electron diffraction pattern. b, HRTEM image.



Extended Data Fig. 5. Broadband nanoindentation relaxation measurements of the $Zr_{55}Cu_{30}Al_{10}Ni_5$ metallic glass. **a**, Thermal drift rate measurements as a function of time on fused quartz. **b**, Typical plot of depth (h) versus time (t) for a nanoindentation relaxation tests on $Zr_{55}Cu_{30}Ni_5Al_{10}$ glass at static 10 mN force for 200 seconds. **c**, **d**, Contact stiffness (**c**) and calculated indentation depth (**d**) as a function of time from a dynamic load relaxation measurement. **e**, Indentation depth as a function of time from nanoindentation relaxation tests. **f**, Nominal shear strain-rate ($\dot{\gamma}$) and shear stress as a function of time in $Zr_{55}Cu_{30}Ni_5Al_{10}$ glass determined by the broadband nanoindentation relaxation experiments.



Extended Data Fig. 6. Nanoindentation Cantilever relaxation measurements of the $Zr_{55}Cu_{30}Al_{10}Ni_5$ metallic glass. a, b, The SEM images of typical $Zr_{55}Cu_{30}Ni_5Al_{10}$ cantilevers with sizes of $5 \times 25 \times 200 \mu m^3$ (a) and $30 \times 70 \times 700 \mu m^3$ (b). **c, d,** The deflection displacements and calculated shear strains are plotted as a function of time under various forces from 1 to 10 mN for $5 \times 25 \times 200 \mu m^3$ cantilevers (c) and $30 \times 70 \times 700 \mu m^3$ cantilevers (d). A magnified plot of the anelastic recovery curves are shown in the insert.

Extended Data Table 1. Fitting parameters for Argon's model at low stresses and CSM model at high stresses in Fig. 2a with equations (1) and (2).

τ / G	$\dot{\gamma}$ (s ⁻¹)	m	V^* (nm ³)	W_{STZ} (eV)	W_0 (eV)	Ω (nm ³)
<0.002	<3×10 ⁻⁶	1	0.028	1.08	1.0	0.22
>0.032	>3×10 ⁻⁴	0.004	0.65	5.75	5.91	5.64

Extended Data Table 2. Physical properties of various glassy materials²⁷⁻³⁴ for normalization in Fig. 2d.

Material	V (m ³ /mol)	T_g (K)	M (g/mol)	ρ (kg/m ³)	τ_c (Pa)
Zr ₅₅ Cu ₃₀ Ni ₅ Al ₁₀	1.19×10^{-5}	695	74.87	6.8×10^3	
Polypropylene	0.22	493	2×10^5	905	
Polystyrene	0.13	464 K	1.26×10^5	966	
Silicate glass	3.3×10^{-5}	818	122	3.7×10^3	9.7×10^7
Polybutadiene	1.19	353	1.07×10^6	900	
Polyethylene	0.022	390	2×10^4	922	
Mayonnaise*	7.7×10^{10}		7×10^4	910	140
Ant aggregation*	2.5×10^{15}		1.5×10^{21}	340	70*

*Mayonnaise, and Ant aggregation data are normalized by τ_c in **Fig. 2d**.

Extended Data Table 3. Area function constants in equation (S1).

C_1	C_2	C_3	C_4	C_5	C_6
24.5	1.05×10^4	-1.34×10^6	1.80×10^7	-5.21×10^7	3.60×10^7

Supplementary Information for

Universal Scaling Law of Glass Rheology

Shuangxi Song¹, Fan Zhu^{1,3} and Mingwei Chen^{2,3*}

Kohlrausch relaxation function fitting

The equivalent shear stress from nanoindentation relaxation tests at room temperature is plotted as a function of time in **Extended Data Fig. 1** deriving from the viscosity data in **Fig. 2b** with Maxwell model. Considering the initial stress as τ_0 , the instant shear stress τ is the product of instant elastic shear strain γ_e and shear modulus G , and the rate changes of stress and strain follow $d\tau = Gd\gamma_e = -Gd\gamma$, where γ is the plastic shear strain whose change is opposite to that of elastic strain ($d\gamma = -d\gamma_e$). The equivalent shear stress from cantilever measurement is used to calculate the time for relaxation at low stress region through **equation (2)** in the main text and **equations (S6) to (S7)**, assuming $\tau \ll \frac{2kT}{V^*}$ and constant

$C = 2c_f v_G \exp\left(-\frac{W_{STZ}}{kT}\right)$ then the transition state theory can be simplified as

$\dot{\gamma} = C \sinh\left(\frac{\tau V^*}{2kT}\right) \cong \frac{C\tau V^*}{2kT}$ at low stress.

$$\frac{d\tau}{dt} = -G\dot{\gamma} \quad (\text{S6})$$

$$t = t_0 - \int_{\tau_0}^{\tau} \frac{2kT}{GC V^*} \frac{d\tau}{\tau} \quad (\text{S7})$$

where t_0 and τ_0 is the start time and stress of Argon shear flow and is taken as 1.6×10^4 s and 1345 MPa in the present study. If we continue to derive the stress as a

function of time following **equations (S8) and (S9)**, the standard single component relaxation function is obtained with relaxation time $t_a = \frac{2kT}{GCV^*}$. **Equation (S9)** is plotted as blue line and fits the experimental data well at low stress range in **Extended Data Fig. 1**.

$$\frac{d\tau}{\tau} = -\frac{GCV^*}{2kT} dt \quad (\text{S8})$$

$$\tau = \tau_0 \exp\left(-\frac{t}{2kT/GCV^*}\right) \quad (\text{S9})$$

On the other hand, the nanoindentation relaxation data at high stress range can be described by CSM theory in Equation (1) and (S10) ¹.

$$W_{CSM} = 4nR\xi G\gamma_c^2 \Omega \left(1 - \frac{\tau}{\tau_c}\right)^n \quad (\text{S10})$$

Where $R=1/4$ is the ‘‘fold ratio’’ and $\xi=3$ is a correlation factor, G is the shear modulus, γ_c is the yield strain, τ_c is the critical stress when W_{STZ} approaches zero ¹. Therefore, the relaxation stress as a function of time for CMS can be derived to be **equation (S11)** following **equation (1)** in the main text and **equations (S3) and (S10)** with relaxation time $t_a = \frac{\eta}{G} = \frac{\tau}{G\dot{\gamma}}$ which is stress dependent.

$$\tau = \tau_c \left[1 - \frac{kT}{W_0} \ln\left(\frac{W_0 G \dot{\gamma}_0}{kT \tau_c} t\right)\right] \quad (\text{S11})$$

The high stress relaxation data follows linear-log relation in **Extended Data Fig. 1** and can be well fitted by **equation (S11)** as green line and the lower limit of relaxation time $t_a(\tau = \tau_c) = \frac{\tau_c}{G\dot{\gamma}_0} = 10^{-13}$ s is also consistent with the phonon relaxation time in metal ($\sim 10^{13}$ Hz) ².

In **Extended Data Fig. 1**, the relaxation data is fitted with CSM model, Kohlrausch relaxation function, and Argon's model as green, dark, and blue lines respectively. It is noticed that the Kohlrausch relaxation function fits well in the transition region.

Universal scaling equation fitting

Following the scaling law at 0 K³, $\tau_0 = 3kT_g/V_0$ and **equation (3)** in the main text can be re-written as

$$\left. \frac{\tau}{\tau_0} \cdot \frac{V}{V_0} = \frac{\eta}{\eta_N} \right|_c \quad (\text{S12})$$

where τ_0 and V_0 are the yield stress and molar volume at 0 K, $\left. \frac{\eta}{\eta_N} \right|_c$ is normalized viscosity at the transition with order of unity. Since the yield stress follows critical-like functional forms with both molar volume (V) and internal energy (U) as follows^{4,5}:

$$\frac{\tau}{\tau_0} = \lambda_V \left(\frac{V_0}{V} - \frac{V_0}{V_J} \right)^{\mu_V} \quad (\text{S13})$$

$$\frac{\tau}{\tau_0} = \lambda_U \left(\frac{U_0}{U} - \frac{U_0}{U_J} \right)^{\mu_U} \quad (\text{S14})$$

where λ_V , λ_U , μ_V , μ_U are constants. V_J and U_J are the critical molar volume and energy of jamming transition at zero stress determined by finite-range potentials, $U = \beta kT$ is the thermal energy where β is a coefficient of order unity, and U_0 is the attractive or bonding energy. When $U_0/kT \gg 1$, such as in attractive colloidal particles, irreversible aggregation results in $V_J \gg V_0$. In most glassy systems including metallic glasses, the packing density is high and the

volume change is small, therefore $\mu_v \approx 1$. On the other hand, for most disordered systems measured at well above 0 K, $U \gg U_j$ and $\lambda_v \left(\frac{U_0}{U} - \frac{U_0}{U_j} \right)^{\mu_v} \approx 1 - \left(\frac{U}{U_0} \right)^c$ which can be well fitted by the yielding of metallic glasses with a temperature dependence as listed in **Data S1**¹. Combining **equations (S13)** and **(S14)**, the four scaled variables can be correlated and the transition boundary is determined by the following **equation (S15)** which is equivalent to **equation (S12)** and universal scaling law **equation (3)**. The experimental data for metallic glasses¹ are plotted as red solid balls at the boundary and can be well fitted by:

$$\frac{\tau}{\tau_0} \cdot \left(\frac{V}{V_0} \right)^{\lambda_v} = 1 - \left(\frac{\beta k T}{U_0} \right)^c \quad (\text{S15})$$

with constants $\beta=0.89$, $c=0.58$, and $\lambda_v = 1$. $U_0=3kT_g$ is the thermal energy required for glass transition at zero stress and maximum density³. At room temperature, the dynamic transition in this Zr-MG occurs at $\tau/\tau_0=0.74$ and $T/T_g=0.42$ and is shown as a red solid ball in **Fig. 3d** with a white dashed line from **equation (S15)**. As shown in **Fig. 3a**, the transition phase diagram depicted by **equations (3)** and **(S15)** is similar to the jamming phase diagram for attractive particles³⁵. MD simulation results of a colloidal dispersion from literature⁴² at $\phi = 0.4$ is plotted as black balls in **Fig. 3d** for comparison.

The dynamic transition boundary for granular systems⁶ under constant driving force or tapping is also plotted as dark gray balls in **Fig. 3**. According to Brown's equation⁷, the system temperature of a glassy system is given by:

$$T = M \overline{u^2} / k, \quad (\text{S16})$$

where $\overline{u^2}$ is the mean square angular velocity of a particle with weight M . The reduced temperature can be re-written as:

$$kT/U_0 = \overline{u^2} \rho / N \tau_c . \quad (\text{S17})$$

Thus, the density or molar volume becomes the accessible experimental quantity in the granular and aggregation systems, unlike the case in metallic and polymer glasses with energy and temperature. Meanwhile, the hard spheres jam to form a solid at a finite packing density at zero stress when kT/U_0 and V_0/V_J is considerable. Under constant stress and limited range of density ($\lambda_v = 1$), the driven variable is replaced by configurational temperature or tap amplitude and density, therefore the transition boundary is described by:

$$\lambda \left(\frac{V_0}{V} - \frac{V_0}{V_J} \right) \cdot \left(\frac{U_0}{\beta kT} - 1 \right)^c = 1 \quad (\text{S18})$$

following **equations (S13) to (S15)**. The glass-liquid transition boundary for a granular tapping system as listed in **Data S2**⁶ can be well fitted by the **equation (S18)** with $\lambda = 0.64$, $U_0 = 3k$, and $V_0/V_J = 0.08$ and is plotted as the blue curve in **Fig. 3b**. The boundary line determined by **equation (S15)** at $\tau/\tau_0 = 0.24$ is also plotted as a red curve in **Fig. 3b** for comparison. The boundaries of these different systems coincide at $V/V_0 \leq 3$ region. However, deviation occurs in the large molar volume range due to the different V_0/V_J in different glassy systems. This divergence is more significant in attractive particles with wide range of packing density and large λ_v ⁴. Thus, the molar volume axis in the phase diagram has to be normalized as $(V/V_0)^{\lambda_v}$ to compare different systems in the volume-stress domain in **Fig. 3c**. For polystyrene gels with $U_0/kT \approx 20$ and $\lambda_v = 3.2$, V_0/V_J approaches zero and equation (S15) can fit well with the boundary data in **Data S3**⁴ and is plotted in **Fig. 3c**. The solid white curve for metallic glasses following equation (S15) with $U_0/\beta kT = 20$ and $\lambda_v = 1$ is also plotted for comparison.

References:

- 1 Johnson, W. L. & Samwer, K. A universal criterion for plastic yielding of metallic glasses with a $(T/T_g)^{2/3}$ temperature dependence. *Phys. Rev. Lett.* **95**, 195501 (2005).
- 2 Pietanza, L. D., Colonna, G., Longo, S. & Capitelli, M. Electron and phonon relaxation in metal films perturbed by a femtosecond laser pulse. *Appl. Phys. A* **79**, 1047-1050 (2004).
- 3 Liu, Y. H. *et al.* Thermodynamic origins of shear band formation and the universal scaling law of metallic glass strength. *Phys. Rev. Lett.* **103**, 065504 (2009).
- 4 Trappe, V., Prasad, V., Cipelletti, L., Segre, P. N. & Weitz, D. A. Jamming phase diagram for attractive particles. *Nature* **411**, 772 (2001).
- 5 Makse, H. A., Johnson, D. L. & Schwartz, L. M. Packing of Compressible Granular Materials. *Physical Review Letters* **84**, 4160-4163 (2000).
- 6 Coniglio, A., de Candia, A., Fierro, A., Nicodemi, M. & Tarzia, M. Statistical mechanics approach to the jamming transition in granular materials. *Physica A: Statistical Mechanics and its Applications* **344**, 431-439 (2004).
- 7 Brown, R. C. II. Brownian motion. *Rep. Prog. Phys.* **5**, 9 (1938).